Journal of Electrical Engineering & Technology
https://doi.org/10.1007/s42835-022-01173-5

INVITED PAPER

Analysis on Noise Source of Claw Pole Machine in Duplex Three-Phase and Belt-Driven System

Jun-Yeol Ryu[1] · Min-Ro Park[2] · Jae-Hyun Kim[1] · Myung-Seop Lim[1]

Received: 6 March 2022 / Revised: 21 June 2022 / Accepted: 27 June 2022

Abstract
The acoustic noise, which is generated in a belt-driven integrated starter and generator (BSG) system, is the recent issue. By many studies, it has been known that the noise can be caused by both radial and tangential components of electro-magnetic force. A duplex three-phase claw pole type machine is widely used in the BSG system. In this case, due to its structural feature and difficulty in control, additional noises at unexpected frequency can be generated. In this paper, a method to analyze noise sources was proposed and applied to a prototype that is the duplex three-phase and claw pole type machine designed for BSG system. First, the electro-magnetic force was calculated by a finite-element analysis considering the unbalanced current measured by the experiment. The obtained force was decomposed according to the frequency and then analyzed. Through the force harmonics, additional noises according to the frequency, which are generated by the unbalanced claw shape in the axial direction and current imbalance between phases, were deduced. Finally, the predicted noise sources were compared with the noise measured through the experiment.

Keywords Belt-driven integrated starter and generator (BSG) · Claw pole type machine · Duplex three-phase · Noise · Vibration

1 Introduction

Electric machines have many advantages such as high-power density and efficiency. In those reasons, the electric machines have been widely used for vehicular components. Despite those advantages, the acoustic noise of the vehicle component is still issue to be overcome in machine design. In many studies, the noise is generally caused by the vibration of the stator, which is generated by the electro-magnetic force [1, 2]. However, there are other noise sources besides the stator vibration caused by the electro-magnetic force, such as vibrations generated by the gearbox, resonance of the mechanical structure, and load fluctuations [3]. And it is hard to clearly separate those mechanical and electro-magnetic noise sources. Therefore, an analysis method for the noise sources is essential to consider the electro-magnetic noise in the design stage.

A belt-driven integrated starter and generator (BSG) machine is operated under the condition that is repeatedly driven and stopped. In a conventional analysis on noise source, because the radial electro-magnetic force is much larger than the tangential component, the only vibration generated by the radial force has been considered [4]. Although it is the widely used method to analyze the noise sources, the predicted vibration has been often different with the experiment result in the belt-driven system. So, the accurate analysis on the noise source is required. Figure 1 shows the noise sources in the belt-driven system. In the figure, the BSG machine is connected to an engine with a belt. The noise sources in the belt-driven system are both radial and tangential components of the electro-magnetic force of the BSG machine because the stator is vibrated by the radial force, and then the vibration of the stator causes the acoustic noise.

✉ Myung-Seop Lim
myungseop@hanyang.ac.kr

Jun-Yeol Ryu
jesus0925@hanyang.ac.kr

Min-Ro Park
minro@sch.ac.kr

Jae-Hyun Kim
zerg1258@hanyang.ac.kr

[1] Department of Automotive Engineering, Hanyang Univerity, Seoul, Korea

[2] Department of Electrical Engineering, Soonchunhyang Univerity, Asan-si, Korea

Published online: 28 July 2022

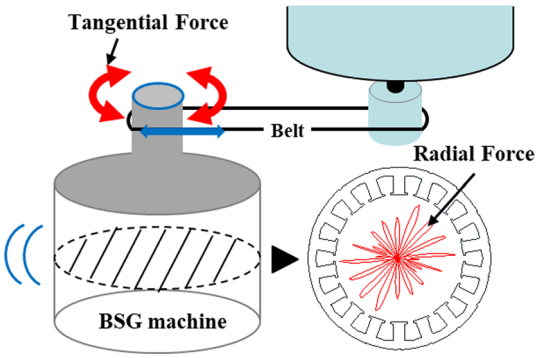

Fig. 1 Noise sources in a belt-driven BSG system

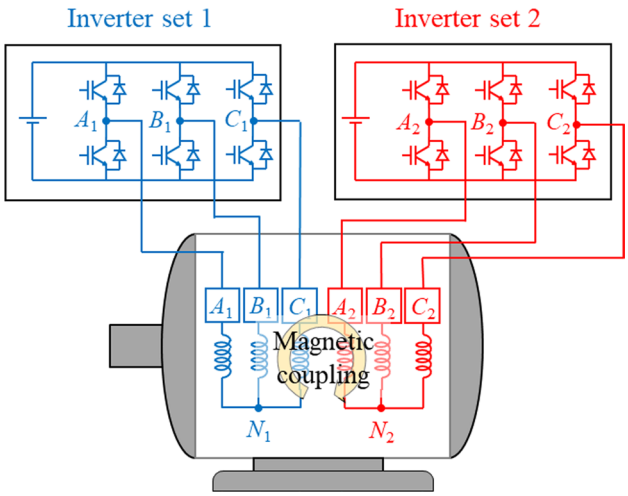

Fig. 2 Structures of duplex three-phase system

Besides, the tangential force, which means a torque ripple, brings out an additional vibration by the belt. In recent studies, the analysis on the noise source including the tangential component of the electro-magnetic force as well as the radial force have been proposed to predict the noise in the belt-driven system [5].

In the consideration of the recent environmental issue, the BSG system should be designed to save the fuel. To improve the energy efficiency, operating performance, and compactness, the duplex three-phase system has been adopted [6, 7]. In the system as shown in Fig. 2, the electric machine is operated with dual inverters. Each three-phase winding set is connected to a respective inverter, and those two sets have an electrical phase difference of 30 degrees. Compared with the three-phase system, the duplex three-phase machine is difficult to control as two sets of three phases are strongly coupled [8]. Under the control with the same carrier frequency, a duplex three-phase system can cause higher current harmonics than the conventional three-phase system because of the control difficulty. So, the current harmonics can be generated in the practical operation. In addition, the current imbalance between phases may occurs. Those current harmonics and imbalance between phases, which are caused by the control difficulty, can generate additional noise.

Due to its robust structure and high reliability, a claw pole type machine is widely used in the BSG system. However, this type of machine also has a deficiency of high acoustic noise because of its structural feature [9]. In this paper, the analysis on the noise source of the claw pole type machine designed for the BSG system was proposed. The analysis process to predict the acoustic noise is as follows. First, a finite-element analysis (FEA) is performed to calculate the electro-magnetic force, which is considered as the excitation source. For more accurate prediction, the current measured by the experiment was considered to calculate the electro-magnetic force. Second, the radial force is decomposed according to the frequency through the spectrum analysis. Besides, the tangential force harmonics are calculated using the harmonic analysis of the torque. Finally, each force harmonic according to the frequency is compared with the noise result measured by the experiment. Through the comparison, the noise sources are classified.

The proposed analysis was applied to a prototype that is claw pole type machine designed for the BSG system. The electro-magnetic force was calculated using the FEA, and it was decomposed according to the frequency. The harmonics according to the frequency were compared with the noise result measured by the experiment. Through the comparison, an additional noise by the structural feature of the claw pole type machine can be determined [10]. Moreover, the effect of torque ripple caused by current harmonics on noise in the belt-driven system was analyzed [11]. Thus, the proposed analysis is suitable to analyze the noise sources of the claw pole type machine designed for BSG and duplex three-phase system. In the next chapter, details of the proposed analysis will be presented.

2 Excitation Source Calculation

Figure 3 shows the proposed analysis procedure to analyze noise sources of the BSG and duplex three-phase system. Its details are as follows.

(1) Current is measured by the experiment to analyze the effect of current harmonics on noise.
(2) Excitation source analysis: the electro-magnetic force is calculated using the FEA.
(3) Spectrum analysis: the radial component of the force was decomposed according to the frequency.
(4) Torque ripple: the harmonics of the torque ripple are calculated using the harmonic analysis.

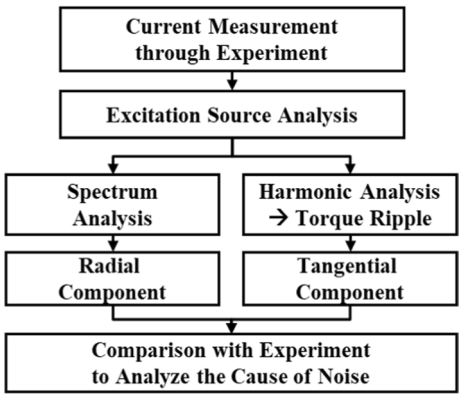

Fig. 3 Process of the proposed analysis on noise source

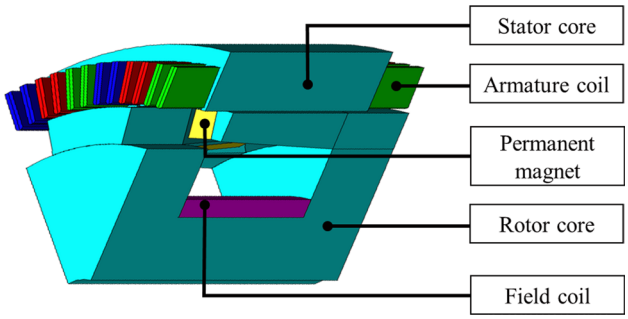

Fig. 4 Prototype of the claw pole type machine designed for BSG system

(5) The obtained excitation sources are compared with the noise measured by the experiment.

The proposed analysis was applied to the prototype designed for the BSG system to predict the noise sources.

2.1 Prototype of the BSG System

Figure 4 shows the prototype of the claw pole type machine designed for the BSG system. Its specifications are presented in Table 1. Because the prototype is the duplex-three phase system, it is operated with two conventional three-phase inverters. The pole and slot number are 16 and 96, respectively. The carrier frequency of the inverter is 10 kHz. At the low-speed region, the prototype is operated with sine-wave drive. On the contrary, it is controlled with the six-step drive control under the high-speed range. The analyses on noise source were conducted at the rotating speed of 2000 rpm and 5200 rpm.

Table 1 Specifications of the prototype

Quantity		Unit	Value
Phase			Duplex 3ph
Pole/slot number			16/96
DC link voltage		V	48
Carrier frequency		kHz	10
Series turn	Armature		15
	Field		150
Permanent magnet	Residual induction	T	1.22
	Recoil permeability		1.05

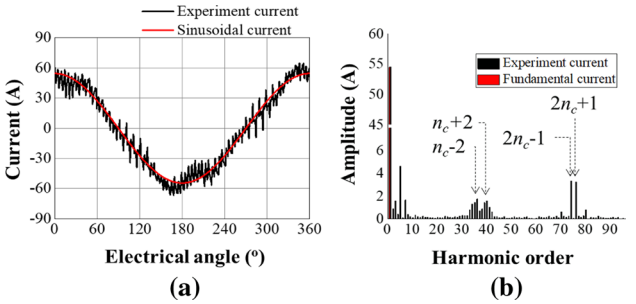

Fig. 5 Input current of phase A, which is measured by the experiment and its fundamental component, at 2000 rpm. **a** the current wave **b** current harmonics

2.2 Electro-Magnetic FEA

To determine the noise caused by the electro-magnetic force, the electro-magnetic FEA was performed to calculate the excitation source of vibration and noise. To consider the effect of current harmonics on noise, the input current of the prototype was measured by the experiment. Figure 5a shows the input current and its fundamental wave at 2000 rpm, where the motor is operated with the sine-wave drive. Those current harmonics are obtained through the harmonic analysis. In Fig. 5b, the current harmonics were presented. At the rotating speed of 2000 rpm, the input frequency is calculated as

$$f = \frac{p}{60} \times \omega_{rpm} \tag{1}$$

where f is the input frequency, p is the pole pair number, and ω_{rpm} is the rotating speed in rpm. The ratio of the input and carrier frequency is presented as follows.

$$n_c = \frac{f_{carrier}}{f} \tag{2}$$

where n_c is the ratio of the input and carrier frequency and $f_{carrier}$ is the carrier frequency. The current harmonics, which are caused by the pulse width modulation (PWM) control,

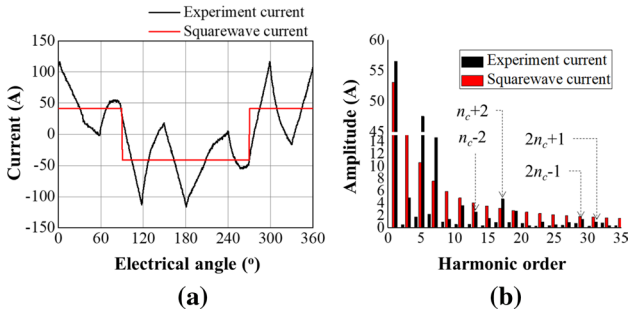

Fig. 6 Input current of phase A, which is measured by the experiment and square wave component, at 5200 rpm. **a** the current wave **b** current harmonics

Table 2 Normalized fundamental components of phase currents

		Rotation speed	
		2000 (rpm)	5200 (rpm)
Set 1	Ph. A	1	0.81
	Ph. B	0.89	0.81
	Ph. C	0.91	0.84
Set 2	Ph. A	1	0.79
	Ph. B	1	0.91
	Ph. C	0.96	1

are generated at the harmonic order of n_c-2, n_c+2, 2n_c-1, and 2n_c+1 [12]. Besides, Fig. 6a shows the current wave at the rotating speed of 5200 rpm. At the speed, the prototype is operated under the six-step drive. In [13], the ideal current form of the six-step drive is the square wave. Figure 6b shows the current harmonics of the input current measured by the experiment and the square wave. To achieve the same power, the amplitude of the square wave was used as the rms value of the experiment current. Table 2 shows the normalized value of the fundamental component of current. There was the current imbalance between phases because the duplex three-phase machine can be hard to control. Moreover, the imbalance at high speed is more severe than at low speed, which can make larger noise in BSG system. Those currents were input to the FEA to obtain the radial and tangential components of the electro-magnetic force.

2.3 Radial Component of Excitation Source

The vibration and noise have been analyzed by the radial force. Because the vibration and noise are generated by the force exerted on the stator, it makes sense that the noise according to frequency is caused by each force harmonics. In this reason, in a conventional spectrum analysis, the radial force is decomposed into spatial harmonic and temporal harmonic components to analyze the sources of the vibration and noise [14, 15].

The electro-magnetic force is generated by interaction of magnetic flux of armature and field. The flux density harmonics of the armature are directly affected by the current harmonics as in Eq. (3)

$$B_{r\_arm} = F_{r\_arm} \times \Lambda = k_w N I_a \times \Lambda \propto \left[\sum_n I_n \cos\left(n \cdot \omega t + \phi_n\right)\right] \times \Lambda \tag{3}$$

where B_{r_arm} is the flux density generated by an armature, F_{r_arm} is the magneto-motive force (MMF) of an armature, Λ is the relative permeance, k_w is the coefficient of the armature winding, N is the series turns of the armature winding, I_a is the armature current, n is the harmonic order, I_n is the amplitude of the current harmonics, ω is $2\pi f$, t is time, and ϕ_n is the phase difference of current harmonics.

The electro-magnetic force is obtained by the Maxwell stress tensor. The radial component of the force density is

$$p_r = \frac{\left(B_r^2 - B_t^2\right)}{2\mu_0} \approx \frac{B_r^2}{2\mu_0} \tag{4}$$

where p_r is the radial force density or electro-magnetic pressure, B_r is the radial component of the air-gap flux density, B_t is the tangential component of the air-gap flux density, and μ_0 is the vacuum permeability. Because the tangential flux density is much smaller than the radial component, the force density is calculated by only the radial component of the air-gap flux density.

In the claw pole type machine, the magnetic field distribution of the air gap is determined by the field, the armature, and the slot effect. When the magnetic saturation of an iron core is neglected, the radial component of the flux density in air gap can be expressed as follows:

$$B_r = \left(B_{r\_field} + B_{r\_arm}\right)\Lambda \tag{5}$$

where B_{r_field} are the slot less flux density by the field. Each term can be expressed using the Fourier series as follows:

$$B_{r\_field} = \sum_\mu B_{m\mu} \cos\left(\mu\omega t - \mu p\theta + \phi_\mu\right) \tag{6}$$

$$B_{r\_arm} = \sum_n \sum_\nu B_{an\nu} \cos\left(n\omega t - \nu p\theta + \phi_{n\nu}\right) \tag{7}$$

$$\Lambda = \lambda_0 \left[1 + \sum_k \Lambda_{ak} \cos\left(ks\theta\right)\right] \tag{8}$$

where $B_{m\mu}$ and $B_{an\nu}$ are the amplitude of the flux density harmonics by the field and by the armature reaction,

respectively, μ is the spatial harmonic order of the air gap magnetic flux density by field and the positive integer, θ is the mechanical angle, ϕ_μ and $\phi_{n\nu}$ are the phase difference of the flux density harmonics by the field and by the armature reaction, ν is the spatial harmonic order of the air gap magnetic flux density by the armature reaction and is determined by the winding, λ_0 is a constant component in the relative permeance, s is the slot number, k is the harmonic order, and Λ_{ak} is the amplitude of relative specific permeance harmonics. In Eq. (9), the method to determine ν is proposed [16, 17].

$$\begin{aligned} &if.\quad f_v = (6k+1)f, \quad \nu = (2mk+1) \\ &if.\quad f_v = (6k-1)f, \quad \nu = -(2mk+1) \end{aligned} \tag{9}$$

where f_ν is the frequency of armature MMF, and m is the number of phases. The radial electro-magnetic force density can be obtained by substituting Eqs. (5)–(8) into (4).

$$p_r = \frac{1}{2\mu_0}\left[\begin{array}{l} \sum\limits_{\mu} B_{m\mu}\cos\left(\mu\omega t - \mu p\alpha + \phi_\mu\right) \\ +\sum\limits_{n}\sum\limits_{\nu} B_{anv}\cos\left(n\omega t - \nu p\alpha + \phi_{n\nu}\right) \end{array}\right]^2 \times\left[1+\sum_k \Lambda_{ak}\cos\left(ks\alpha\right)\right]^2 \tag{10}$$

From Eq. (10), the vibration order and frequency of the radial component of force are summarized in Table 3. Through the equations, the vibration sources at a specific frequency can be analyzed. For example, the armature current is sinusoidal ($n=1$), when μ is 1, the force of $2f$ frequency component occurs. Therefore, the excitation sources, which is radial force density, of the claw pole type machine can be analyzed based on the same equations.

Figure 7 shows the example of spectrum analysis result of the radial force density at 2000 rpm. Because of the unbalance of the claw shape along the axial position, the flux density distributions according to the axial position are different, which brings out diverse force density harmonics according to the axial position. In this reason, the force density was calculated with the flux density extracted at two positions as shown in Fig. 7a, which is line A and B is 1.5 and 10.5 mm apart from center, respectively. Figure 7b and c is the spectrum analysis results at line A and B, respectively.

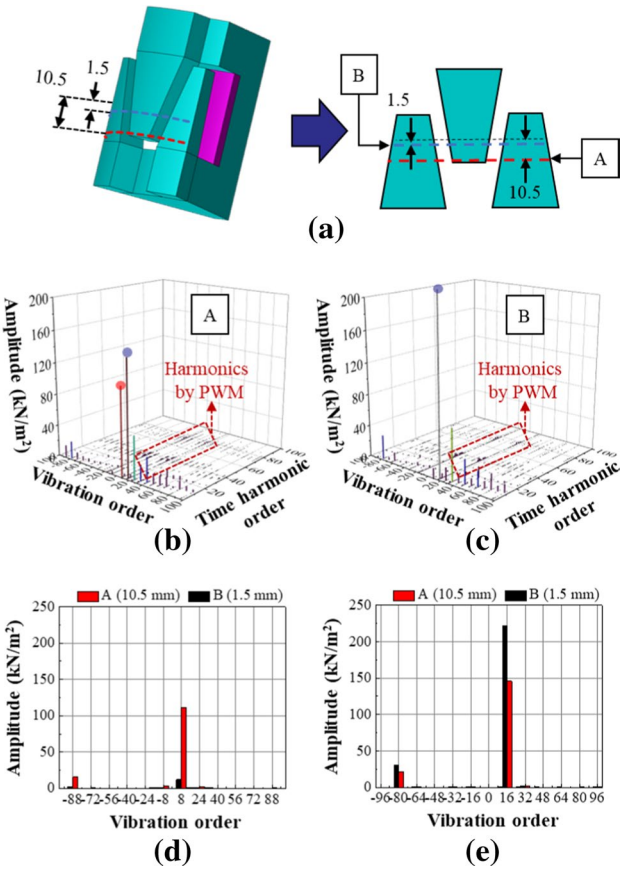

Fig. 7 Spectrum analysis results at 2000 rpm. **a** position where force density is extracted. **b** spectrum analysis result at the end side of the claw (line A). **c** spectrum analysis result at the center of the claw (line B). **d** force density at 1*f*. **e** force density at 2*f*

In the result at line A, dominant harmonics are generated at 1*f* and 2*f*, and those amplitudes are presented in Fig. 7d, e and Table 4. At line B, the force density of the vibration order $r=16$ is generated by the interaction between $\mu=1$ component of the flux density by the field and the $\nu=1$ component of the armature reaction at the air gap, which is commonly generated in 16-poles and 96-slots model. On the other hands, the force density of $r=8$ at 1*f*, which is a half of the pole number, is rarely generated in other types of motors. Though the force density of $r=8$ is about half that of $r=16$ component, the deformation of stator generated by

Table 3 Vibration order and frequency of radial electromagnetic force

Source	Vibration Order (r)	Spatial order
Field	$p(\mu_1 \pm \mu_2)$	$(\mu_1 \pm \mu_2)$
Armature	$p(\nu_1 \pm \nu_2)$	$(n_1 \pm n_2)$
Interaction of field and armature	$p(\mu \pm \nu)$	$(\mu \pm n)$
Interaction of field and stator slotting	$p(\mu_1 \pm \mu_2) \pm ks$	$(\mu_1 \pm \mu_2)$
Interaction of armature and stator slotting	$p(\nu_1 \pm \nu_2) \pm ks$	$(n_1 \pm n_2)$

Table 4 Spectrum analysis result @ 2000 rpm

Axial position	Temporal harmonic	Minimum vibration order	Force density (kN/m^2)
End of claw (line A)	1*f*	8	111.3
	2*f*	16	145.7
Center of claw (line B)	1*f*	8	12.1
	2*f*	16	221.3

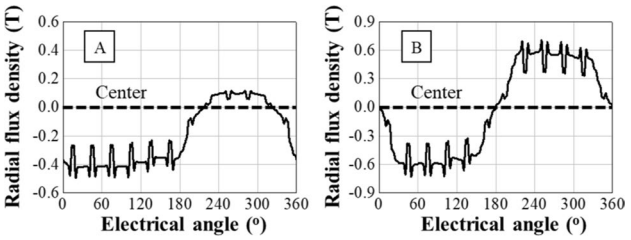

Fig. 8 Flux density extracted at 2000 rpm. (Left: flux density extracted at line A, 10.5 mm apart from the center. Right: flux density extracted at line B, 1.5 mm apart from the center)

the force density of $r=8$ can be larger. The deformation of the stator is determined by Eq. (11).

$$\frac{1}{r^4} \propto d \tag{11}$$

where d is the deformation of the stator. So, it means that the electro-magnetic force density of the minimum vibration order is the main vibration and noise source. As mentioned before, the component of $r=8$ at 1*f* is generated at the end side of the claw. Because the claw has the unbalanced width along the axial position, the offset component of flux density occurs as shown in Fig. 8. Due to the structural feature of the claw pole type machine, the radial flux density by the field of Eq. (6) is changed as follows:

$$B_r = B_0 + \sum_k B_k \cos\left(k\omega t + \phi_k\right) \tag{12}$$

where B_0 is the offset component of the flux density and ϕ_k is the phase of the k^{th} flux density harmonics. The spatial harmonic order of the B_0 is zero. So, the force density of the vibration order $r=8$ is generated by the interaction between components of the $\mu=0$ component and the $\nu=1$. In addition, because the temporal harmonic order of B_0 is $n=0$, the force density is generated at 1*f*. Although only the results at 2000 rpm were presented in this chapter considering the space limit, the spectrum analysis results at 5200 rpm has the same trend of force density harmonics. Therefore, the minimum vibration order of the radial force density is essential to predict the vibration of stator, and the proposed method can provide a theoretical approach to obtain noise sources of the claw pole type machine.

2.4 Tangential Component of Excitation Source

Because the vibration can be generated by the torque ripple in the belt-driven system, the harmonics of the vibration are matched with the torque ripple harmonics in this chapter. The torque ripple, which is determined based on the current harmonics, is expressed as

$$T(t,\theta) = \frac{1}{\omega}\sum_m e_m(t,\theta)\cdot i_m(t,\theta) \tag{13}$$

where T is the torque, m is the phase, e_m is the induced voltage of phase m and i_m is the current of phase m. The torque ripple is affected by the current harmonics of all phases. In the duplex three-phase system, the current harmonics of phases are represented as follows:

$$F_a(t,\theta) = \sum_{m=1}^{3}\left\{\begin{array}{l} NI_n \sin\left(\omega t - \dfrac{2(m-1)\pi}{3}\right) \\ \times \displaystyle\sum_n \cos\left(n\left(\theta - \frac{2(m-1)\pi}{3}\right)\right) + \\ NI_n \sin\left(\omega t - \dfrac{\pi}{6} - \dfrac{2(m-1)\pi}{3}\right) \\ \times \displaystyle\sum_n \cos\left(n\left(\theta - \frac{\pi}{6} - \frac{2(m-1)\pi}{3}\right)\right) \end{array}\right\} \tag{14}$$

where F_a is the armature MMF generated by currents of phases and I_n is the amplitude of the nth current harmonic. Using the angle addition and subtraction formulas, the Eq. (14) can be simplified as:

$$\begin{aligned} F_a(t,\theta) \propto & \sum_{m=1}^{3}\sin\left\{\omega t + n\theta + (n+1)\frac{2(m-1)\pi}{3}\right\} \\ & + \sum_{m=1}^{3}\sin\left\{\omega t - n\theta + (n-1)\frac{2(m-1)\pi}{3}\right\} \\ & + \sum_{m=1}^{3}\sin\left\{\omega t + n\theta + (n+1)\frac{2(m-1)\pi}{3} - \frac{\pi}{6}(n+1)\right\} \\ & + \sum_{m=1}^{3}\sin\left\{\omega t - n\theta + (n-1)\frac{2(m-1)\pi}{3} + \frac{\pi}{6}(n+1)\right\} \end{aligned} \tag{15}$$

The above equation of the armature MMF is determined by the harmonic order as follows:

$$F_a(t,\theta) = \begin{cases} 0 & at\ \{(n+1) \neq 12l\} \\ \neq 0 & at\ \{(n+1) = 12l\} \end{cases} \tag{16}$$

where n and l are integer. It means that under the condition that all phases are in balance, only a torque ripple of a multiple of twelve is generated regardless of the current harmonics.

Figure 9 shows the torque wave and torque ripple at 2000 rpm and 5200 rpm. The torques was calculated with the current measured by the experiment and its basic form in Figs. 5 and 6. Theoretically, the torque ripple in the duplex three phase system should be generated at 12f, 24f and 36f as presented in Eq. (16). However, additional harmonics of the torque ripple were generated at 1f and 2f. Such harmonics indicate that the currents between phases are unbalanced. The torque wave under the current unbalance is obtained as follows:

$$\begin{aligned} T(t) &= \frac{1}{\omega} e(t) \cdot i(t) \\ &= \frac{1}{\omega}\left[\sum_k E_k \cos\left(k\omega t + \phi_k\right) \sum_l I_l \cos\left(l\omega t + \phi_l\right)\right] \\ &= \frac{1}{2\omega}\left[\sum_k \sum_l E_k I_l \cos\left((k \pm l)\omega t + \phi_{kl}\right)\right] \end{aligned} \quad (17)$$

where E_k and I_l are harmonics of the induced voltage and current, respectively, k and l are harmonic order, ϕ_k, ϕ_l, ϕ_{kl} are phase of induced voltage, current, and torque ripple, respectively. If a fundamental component of the induced voltage is considered, the torque ripple harmonics generated by the unbalanced current is presented in Eq. (18).

$$T(t) = \frac{1}{2\omega}\left[\sum_l E_1 I_l \cos\left((1 \pm l)\omega t + \phi_{kl}\right)\right] \quad (18)$$

where E_1 is the fundamental component of the induced voltage. So, the first and second current harmonics, that are generated when the current between phases are unbalanced, brings out torque ripple at 1f and 2f. Therefore, the current unbalance between phases can affect the noise and vibration in the belt-driven system.

3 Comparison Between Noise Source and Experiment

The noise sources, such as the radial and tangential force density, were compared with the noise results which were measured by the experiment. The experiment set is shown in Fig. 10. The prototype was connected to dynamometer through the torque transducer and belt. Under the load torque of 6 Nm, the noises were measured with microphone which are placed on the side of the prototype as shown in Fig. 11. The measured overall noise according to the rotating speed and waterfall plot are below reported in Figs. 12 and 13. The prototype is operated with sine-wave drive under 2000 rpm and with the six-step drive under 5200 rpm, respectively. In the overall noise result, the noise increases according to speed. And the noise at the speed of 5200 rpm is the most severe. The noise cause can be analyzed through the waterfall plot. In the waterfall, the dominant noise sources at 1f, 2f, and 12f were selected considering the noise amplitude.

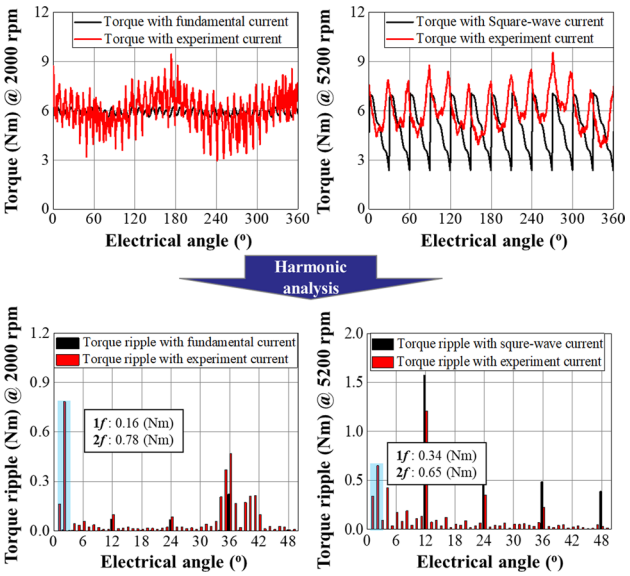

Fig. 9 Torque wave and its torque ripple at 2000 rpm and 5200 rpm. (Load torque: 6 Nm)

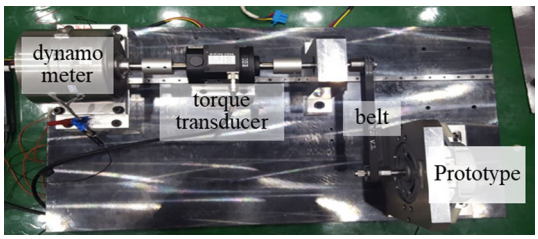

Fig. 10 Experiment setup of the belt-driven system

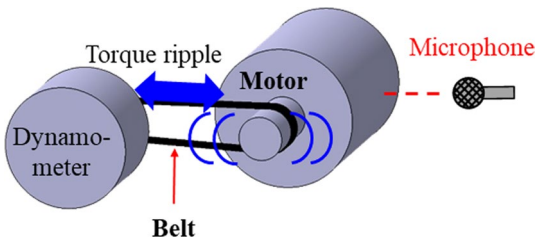

Fig. 11 Noise measurement of the reference BSG motor

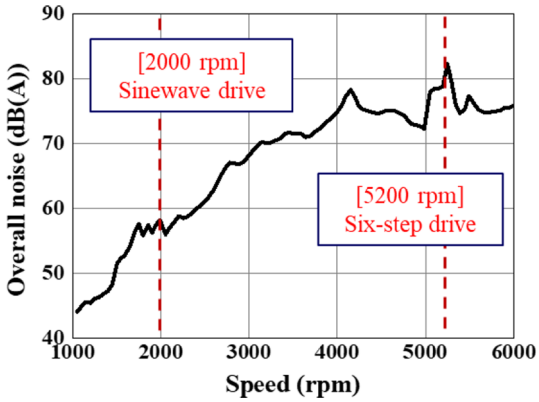

Fig. 12 Overall noise measurement of the reference BSG motor under the load condition (load torque is 6 Nm)

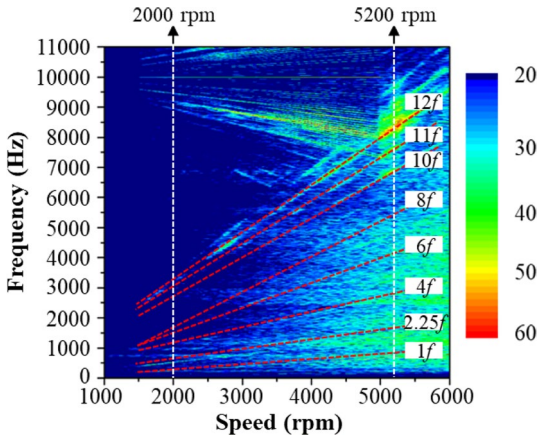

Fig. 13 Waterfall plot of the reference BSG motor under the load condition (load torque is 6 Nm)

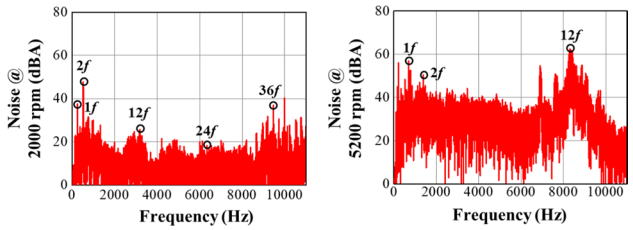

Fig. 14 The noise according to frequency measured by the experiment

Especially, the maximum noise is generated at the speed of 5200 rpm, and its main noise source is 12*f* component. Each noise result at 2000 rpm and 5200 rpm is shown in Fig. 14. In the results, the multiples of the input frequency were determined. Among the frequencies, 1*f* and 2*f*, which can cause the critical vibration, were selected, and the frequency at 12*f, 24f and* 36*f* was chosen because it is a

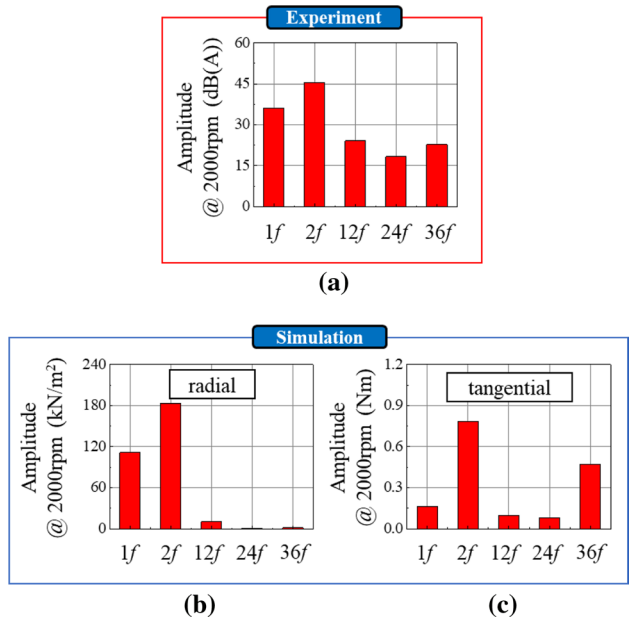

Fig. 15 Comparison between simulation and experiment at 2000 rpm. **a** Noise amplitude of experiment. **b** Radial force density harmonics according to the frequency. **c** Tangential force density harmonics according to frequency

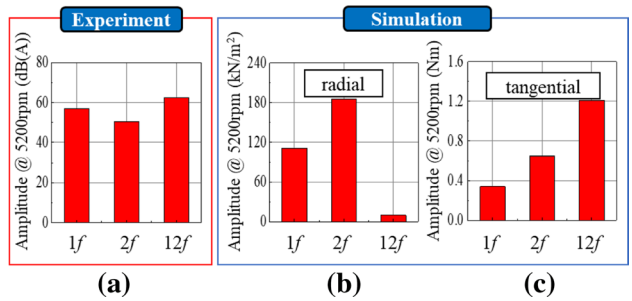

Fig. 16 Comparison between simulation and experiment at 5200 rpm. **a** Noise amplitude of experiment. **b** Radial force density harmonics according to the frequency. **c** Tangential force density harmonics according to frequency

common component in the duplex three-phase system. The human audible frequency is from 20 to 20,000 Hz, and the frequency of 36*f* component at 5200 rpm is 24960 Hz, which is outside this range. So, the target frequencies at 5200 rpm were determined only for 1*f*, 2*f*, and 12*f*.

Figures 15 and 16 show the comparison between the noise measured by the experiment and the noise sources obtained through the simulation at 2000 rpm and 5200 rpm, respectively. And those values are presented in Tables 5 and 6. In Fig. 15b and Fig. 16b, those noise sources are the radial force density. Among the results, the radial force density at 1*f* is generated because of the structural feature of the claw pole type machine, which can be the dominant noise

Table 5 Comparison between noise sources obtained by simulation and noise measured by experiment at 2000 rpm

	Experiment (dB(A))	Radial component (kN/m^2)	Tangential component (Nm)
1*f*	36.1	111.3 ($r=8$)	0.16
2*f*	45.6	183.5 ($r=16$)	0.78
12*f*	24.1	10.3 ($r=96$)	0.10
24*f*	18.3	0.9 ($r=96$)	0.08
36*f*	22.8	1.6 (r=96)	0.47

Table 6 Comparison between noise sources obtained by simulation and noise measured by experiment at 5200 rpm

	Experiment (dB(A))	Radial component (kN/m^2)	Tangential component (Nm)
1*f*	56.9	110.7 ($r=8$)	0.34
2*f*	50.3	185.5 ($r=16$)	0.65
12*f*	62.4	9.9 ($r=96$)	1.21

source when its vibration order is minimum. Besides, the tangential component of force density, which is harmonics of torque ripple, are presented in Fig. 15c and Fig. 16c. As forementioned in Eq. (16), the torque ripple at 12*f,* 24*f* and 36*f* is commonly generated in duplex three-phase system. However, the harmonics of the torque ripple at 1*f* and 2*f* can be generated by the unbalanced current between phases of armature windings. In Fig. 15 and Table 5, although the magnitude of the excitation source does not necessarily mean the amplitude of noise because of the mechanical properties, the noise sources at dominant frequencies can be analyzed. Through the comparison, the noise sources of the claw pole type BSG machine can be obtained and analyzed by the proposed method.

4 Conclusion

This paper proposes the analysis on noise sources of claw pole type machine designed for the BSG and duplex three-phase system. From the noise, which is measured by the experiment, the target frequencies for the analysis were determined as 1*f*, 2*f*, and a multiple of twelve. The noise sources, which are the radial component of the electromagnetic force density and torque ripple, were calculated using the FEA. To consider the practical control, the FEA was performed with the input current measured by the experiment. The obtained radial force density was decomposed into spatial and temporal harmonics through the spectrum analysis. Besides, the harmonic analysis of the torque ripple was performed. Those noise sources were compared with the noise measured by the experiment. Through the comparison, the following conclusions were deduced. Because the torque ripple can bring out the vibration and noise in the belt-driven system, the noise at a multiplex of 12*f* is generated by the torque ripple. The noise sources at 1*f* and 2*f* are affected by both the radial and tangential components of the force density. The radial force density at 1*f* is inevitably generated due to the structural feature in claw pole type machine. Besides, the noise sources of the torque ripple at 1*f* and 2*f* can be generated by the unbalanced current between phases, which can easily occur in the duplex three-phase system. Thus, more attention to control for input current and balance between phases is required in belt-driven system. In those reasons, the noise sources can be analyzed by the proposed method. It is also expected to be used to deal with the acoustic noise at a specific frequency in the belt-driven and duplex-three phase system.

Acknowledgements This work was supported by the National Research Foundation of Korea (NRF) Grant funded by the Korea government(MSIT) (No. NRF-2020R1A4A4079701).

References

1. Islam R, Husain I (2010) Analytical model for predicting noise and vibration in permanent-magnet synchronous motors. IEEE Transa Ind Appl 46(6):2346–2354
2. Sun T, Kim J, Lee G, Hong J, Choi M (2011) Effect of pole and slot combination on noise and vibration in permanent magnet synchronous motor. IEEE Trans Magn 47(5):1038–1041
3. Lahouasnia N, Rachedi MF, Drici D et al (2020) Load unbalance detection improvement in three-phase induction machine based on current space vector analysis. J Electr Eng Technol 15:1205–1216
4. Jang I et al (2014) Method for analyzing vibrations due to electromagnetic force in electric motors. IEEE Trans Magn 50(2):297–300
5. Kim D-Y, Park M-R, Sim J-H, Hong J-P (2017) Advanced method of selecting number of poles and slots for low-frequency vibration reduction of traction motor for elevator. IEEE/ASME Trans Mechatron 22(4):1554–1562
6. Kim TH (2019) The effect of different arrangements of stator windings on iron losses in a dual three-phase 12-slot 10-pole BLAC motor. J Electr Eng Technol 14:1281–1286
7. Nekoubin A, Soltani J, Dowlatshahi M (2020) Comparative analysis of three-phase and five-phase permanent-magnet motor based on finite element method. J Electr Eng Technol 15:1705–1712
8. Kong W, Guo H, Tang G et al (2020) Optimized non-sinusoidal power supply in high-power multiphase induction motor drive based on harmonic parameter analysis. J Electr Eng Technol 15:2627–2638
9. Ryu J-Y, Park M-R, Kim J-H, Lim M-S (2021) Analysis on noise source of claw pole machine in belt-driven system. In: 2021 24th international conference on electrical machines and systems (ICEMS), pp. 1440–1444
10. Wu S, Zuo S, Wu X, Lin F, Zhong H, Zhang Y (2017) Vibroacoustic prediction and mechanism analysis of claw pole alternators. IEEE Trans Industr Electron 64(6):4463–4473

11. Jiang S, Zhong Z (2021) Coupling harmonic voltages considered harmonic currents injection method for torque ripple reduction. J Electr Eng Technol 16:2119–2130
12. Tang L, Ruan J, Ding H et al (2020) Analysis of transient magnetic force on end-winding in the inverter-fed induction machine. J Electr Eng Technol 15:235–243
13. Yazdan T, Zhao W, Lipo TA, Kwon B-I (2016) A novel technique for two-phase BLDC motor to avoid demagnetization. IEEE Trans Magn 52(7):1–4
14. Wang S, Li H (2020) Reduction of electromagnetic vibration and noise in permanent magnet motor for EVs by optimizing design of rotor based on GPR-PSO model. J Electr Eng Technol 15:1231–1243
15. Xing Z, Wang X, Zhao W (2021) Analysis and reduction of electromagnetic force waves of permanent magnet synchronous motors considering rotor eccentricity. J Electr Eng Technol 16:3047–3059
16. Park M-R, Jung J-W, Kim D-Y, Hong J-P, Lim M-S (2019) Design of high torque density multi-core concentrated flux-type synchronous motors considering vibration characteristics. IEEE Trans Ind Appl 55(2):1351–1359
17. Yang Z, Li W, Gou Y et al (2020) Research on radial force of permanent magnet synchronous motor based on maxwell. J Electr Eng Technol 15:2601–2608

Jun-Yeol Ryu He received the Bachelor's degree in mechanical engineering and electronic systems engineering from Hanyang University, Ansan, South Korea, in 2016. He is currently pursuing the Ph. D degree in automotive engineering with Hanyang University, Seoul, South Korea. His research interests include design and optimization of electric machines and analysis of electromagnetic field.

Min-Ro Park He received the bachelor's degree in electrical engineering from Chungnam National University, Daejeon, South Korea, in 2013 and the integrated master's and Ph.D. degrees in automotive engineering from Hanyang University, Seoul, South Korea, in 2020. From 2020 to 2022, he was a Senior Researcher in Korea Institute of Robotics and Technology Convergence (KIRO), Pohang, South Korea. Since 2022, he has been with Soonchunhyang University, Asan, South Korea, where he is currently an Assistant Professor. His research interests include multi-physics analysis and design of electric machine for mechatronics systems.

Jae-Hyun Kim He received the bachelor's degree in mechanical engineering, in 2017, from Hanyang University, Seoul, South Korea, where he is currently working toward the Ph. D. degree in automotive engineering. His research interests include the design, and the analysis of vibration and noise of electric machines.

Myung-Seop Lim He received the Bachelor's degree in mechanical engineering from Hanyang University, Seoul, South Korea, in 2012. Also, he received the Master's and Ph.D. degree in automotive engineering from the same university, in 2014 and 2017, respectively. From 2017 to 2018, he was a Research Engineer in Hyundai Mobis, Yongin, South Korea. From 2018 to 2019, he was an Assistance Professor in Yeungnam University, Daegu, South Korea. Since 2019, he has been with Hanyang University, Seoul, South Korea, where he is currently an Assistant Professor. His research interests include electromagnetic field analysis and electric machinery for mechatronics systems.